Kinetics, nanomechanical and tribological characterizations of Fe_2B layers on ASTM A29 steel

Martin Ortiz-Domínguez[1], Mourad Keddam[2]

[1]Autonomous University of Hidalgo State, Escuela Superior de Ciudad Sahagún-Mechanical Engineering, Carretera Otumba-Cd. Sahagún No. 7, Colonia Legaspi, Zona Industrial, Ciudad Sahagún 43998, Hidalgo, Mexico,
E-mail: martin_ortiz@uaeh.edu.mx

[2]Laboratoire de Technologie des Matériaux, Faculté de Génie Mécanique et Génie des Procédés, USTHB, B.P. No. 32, 16111 El-Alia, Bab-Ezzouar, Algiers, Algeria,
E-mail: mkeddam@usthb.dz

(Received 18 February 2026; Accepted 29 May 2026)

Abstract:

This work investigates the application of the pack-boronizing process to a low-alloy steel of type ASTM A29 within the temperature range 1123-1273 K. Microscopic observations revealed the formation of a single Fe_2B layer at all processing temperatures, with a less pronounced toothed interfacial morphology. The tribological behaviour of the boride layers was studied using pin-on-disc tests, and their nanomechanical properties, such as elastic modulus and nanohardness, were evaluated by nanoindentation tests. Furthermore, the Taylor expansion (TE) model was implemented to assess boron diffusivities in Fe_2B, from which the activation energy was determined. The empirical verification of this approach has been made employing four additional boriding conditions.

Keywords: Boriding. Kinetics, Tribology, Nanomechanical properties, Taylor expansion model, Activation energy.

1. Introduction

Among thermochemical treatments, powder boriding is notable for its low cost, simple industrial implementation, and remarkable tribological properties. During boriding, boron atoms diffuse into the alloy surface and react with the base metal to form a dense, hard

boride layer strongly bonded to the substrate. This layer markedly improves wear, corrosion, and oxidation resistance.

Studies [1–3] show that boride coatings exhibit significantly lower abrasion and erosion rates than other surface treatments. Compared with carburized, nitrided, or coated steels (such as Cr, Ni, Cr_3C_2, CrB, NiCrBC, TiN or WC), borided steels exhibit superior performance.

Due to their high thermal and chemical stability, boride layers retain their integrity under severe conditions, making them suitable for pumps, valves, molds, cutting tools, and wear-resistant machine parts. Consequently, pack-powder boriding is a cost-effective and efficient surface modification technique that improves metallic component durability. It reduces energy consumption and wear-related costs [4–9]. In iron-based alloys, this treatment forms the iron borides FeB and Fe_2B. Their relative proportions depend strongly upon the processing conditions and the chemical composition of substrate. Because of its properties, a single Fe_2B layer [9] is generally preferred over a bilayer (FeB + Fe_2B) for industrial use [10]. This is because the (FeB/Fe_2B) interface can act as a weak point, prone to cracking under mechanical or thermal stress, reducing the service life.

The Fe_2B phase has a tetragonal crystal structure and presents high hardness, excellent wear resistance, thermal stability, and a low friction coefficient, making it suitable for components exposed to abrasive wear and dynamic loading. Therefore, precise control of boriding parameters is required to obtain a uniform, strongly adherent single-phase layer.

In industry, ASTM A29 steel is a high-strength alloy known for its hardness, wear resistance, fatigue resistance, and thermal stability. It is particularly suited for bolts, bearings, gears, camshafts, racks, and other components under severe mechanical conditions. However, the surface properties of ASTM A29 steel can be significantly improved by boriding. Recently, diffusion-based mathematical models have been suggested to analyze the boriding kinetics of Fe_2B layers on different metallic alloys [11–16]. In deterministic models, the system behaviour is entirely ruled by diffusion laws and predefined physical parameters. These approaches are generally based on the solution of Fick's laws and the mass balance equations. Therefore, the mass transfer of B atoms can be described using either analytical or numerical formulations. Non deterministic models, such as fuzzy logic systems, artificial neural networks, and dimensional analysis approaches, are

based on approximations rather than pure physical equations. In these models, the relationships between input processing parameters and the output variable can be obtained by using artificial intelligence techniques or statistical tools. To illustrates this, Keddam et al. [11] implemented the Taylor expansion model to investigate the growth kinetics of Fe_2B layers formed on S235 steel. This recent kinetic approach offers significant advantages over conventional diffusion models because it provides a simplified formulation of the diffusion problem together with an exact analytical solution. In this approach, the B concentration profile across the Fe_2B layer is represented by a Taylor series expansion around the moving growth interface. The model is established by solving the diffusion problem through an ordinary differential equation formulation. In another study, Ramadan et al. |12] developed a phase-field-based model to investigate the crystallographic orientation of iron boride needles formed during the boriding process. The model incorporated the competitive growth behaviour of boride needles and their preferential orientation by accounting for interfacial energy effects. In addition, the study revealed that the textured growth of boride needles does not depend upon the initial crystal size. Campos-Silva et al. |13] applied the mean diffusion coefficient model for the boriding kinetics of AISI 1018 and AISI 4140 steels, where a single Fe_2B layer was produced on the surface. The model assumes a linear boron concentration profile inside the Fe_2B layer, while boron mobility is represented by an effective constant diffusion coefficient averaged over the layer thickness. This parameter can be evaluated from the experimentally measured parabolic growth constants. By using non deterministic approaches, Campos et al. [14] modelled the Fe_2B layer growth kinetics in the case of AISI 1045 steel employing both Mamdani and Takagi-Sugeno fuzzy logic approaches. Membership functions were defined to fuzzify the input variables and to represent the output in terms of layer thickness. The system architecture is based upon two input membership functions and a single output variable. Both approaches involve fuzzification, membership functions, and rule-based reasoning. However, the Takagi–Sugeno method is generally more appropriate for precise modelling and large-scale systems, whereas the Mamdani approach generates fuzzy outputs that must be converted into a crisp value, unlike Takagi–Sugeno method, which handles mathematical functions to generate the output. Ortiz-Dominguez et al. [15] proposed two approaches for modelling the growth kinetics of Fe_2B layers on AISI 1018 steel. The first kinetic approach used the

mass balance equation at the growing interface under a steady-state diffusion regime. The dimensional analysis model was implemented in the range of 1123 to 1273 K. The main advantage of this latter approach lies in reducing the number of physical variables into dimensionless groups using the Buckingham-Pi theorem. This method therefore constitutes an alternative to deterministic diffusion models. Finally, Ortiz-Dominguez et al. [16] applied both the integral method, based on the solution of differential–algebraic equations, and the mean diffusion coefficient model to predict the growth kinetics of Fe_2B layers on AISI 4147 steel. The integral method differs from classical diffusion models in its mathematical formulation. To sum up, all these models enable reliable and accurate predictions of layer thickness evolution and therefore constitute essential tools for the design, optimization, and automation of boriding processes in modern industrial applications. The aim of this study is to examine the boriding behaviour of ASTM A29 steel using the solid boriding process within the temperature range 1123–1273 K. The resulting surface layers were characterized by scanning electron microscopy (SEM) coupled with energy-dispersive spectroscopy (EDS). The hardness of the formed boride layers was evaluated, and their wear performance was investigated through pin-on-disc wear testing. In addition, nanoindentation experiments were conducted to determine the nanohardness and elastic modulus of the Fe_2B layers. Lastly, the Taylor expansion model [11] was implemented to determine the B activation energy in Fe_2B and to experimentally validate it.

2. Materials and Methods

2.1 Steel grade and boriding treatment

The nominal chemical composition of the ASTM A29 steel for experiments is given (in wt. %) in Table 1.

Table 1 *Chemical composition of ASTM A29 steel expressed in weight percent (wt.%)*

Element (in wt.%)	C	Mn	Si	Cr	Mo	P	S

ASTM A29 steel	0.48 - 0.53	0.75–1.0	0.15–0.30	0.80–1.10	0.15–0.25	-	-

Cubic samples (10 × 10 × 10 mm^3) were cut from commercial square bars using a precision cutting machine. Before boriding, the sample surfaces were ground with silicon carbide papers of various grit sizes to obtain a uniform finish. The substrates were then subjected to the powder-pack boriding at different processing parameters which are 1123, 1173, 1223 and 1273 K for a treatment time up to 8 h. They were placed into a heat-resistant stainless steel container and embedded in powders mixture (Figure 1). The boriding medium consisted of 33.5 wt.% B_4C as the boron donor, 5.4 wt.% KBF_4 as the activator, and 61.1 wt.% SiC as the inert diluent. At elevated temperatures, KBF_4 thermally decomposes, promoting the formation of active boron-containing species that enhance boron diffusion toward the steel surface. After the boronizing the specimens were slowly cooled to ambient temperature.

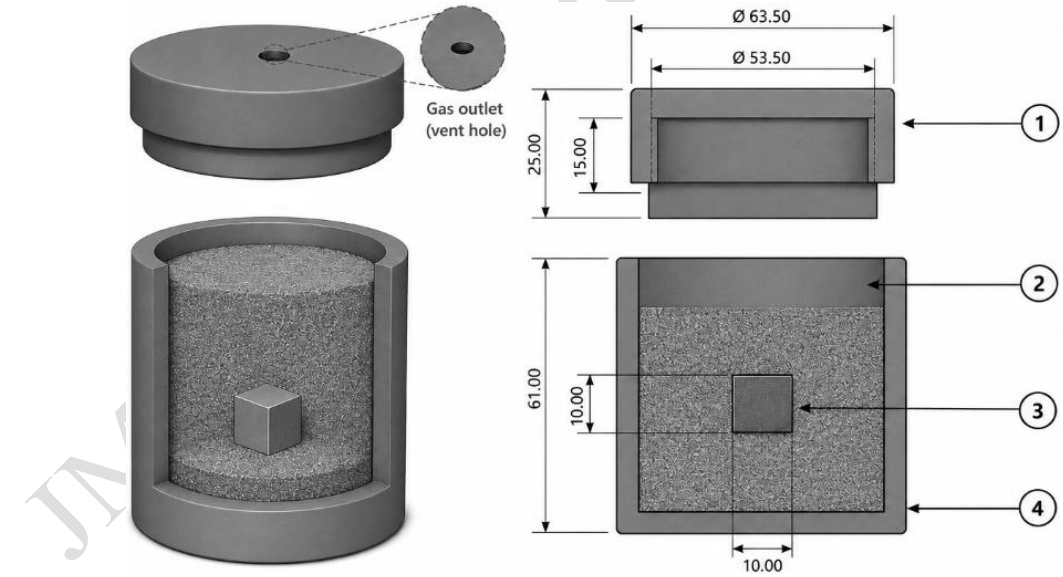

Figure 1. *Experimental setup used for the pack-boriding treatment. It includes: (1) a lid with a small opening for the release of gaseous species, (2) the powder mixture used, (3) the sample to be treated, and (4) the main cylindrical body of the container. All dimensions are given in mm.*

2.2 Experimental techniques

The cross-sectional metallographic samples were prepared according to standardized methods, i.e. grinding by a set of emery papers, which was followed by polishing by using diamond suspensions with particle sizes of 0.25 μm and 0.05 μm. Each polishing stage was conducted for 20 min to obtain a mirror-like surface suitable for accurate microstructural characterization. After every polishing step, the samples were thoroughly cleaned in an ultrasonic acetone bath for 30 s in order to eliminate residual contaminants and ensure optimal surface conditions. The cross sections of borided samples were chemically etched using a Nital solution (4 Vol.%) to examine the microstructures in detail. The Fe_2B layer thickness was measured using both a VHX-7000 4K optical microscope and a JEOL JSM-6510IV scanning electron microscope coupled with energy-dispersive spectroscopy (EDS), and enabling detailed observation at different magnification levels. Quantitative evaluation of the Fe_2B layer thickness was performed using Image-Pro Plus v.10.0 software through an automated image analysis approach, ensuring high objectivity and reproducibility of the measurements. The mean values of Fe_2B layers were obtained based on 150 measurements according to the practical method proposed by Kunst and Schaaber [17]. These measurements were taken from each of the 32 cross-sections of the treated samples, resulting in robust and highly reliable thickness data. Figure 2 illustrates the metallographic preparation and characterization procedure employed before and after the boriding treatment.

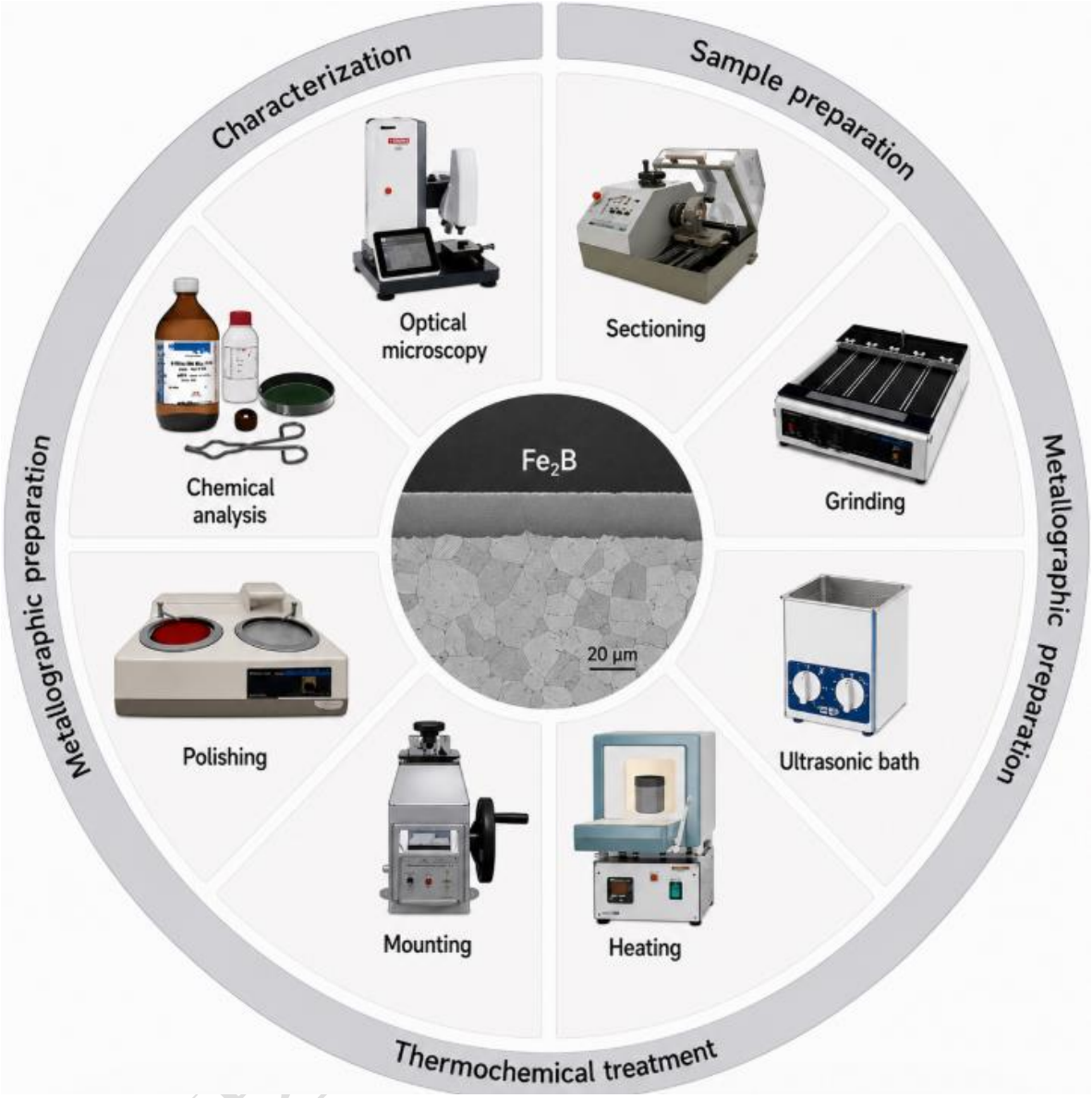

***Figure 2**. Schematic representation of the experimental methodology employed for the preparation, thermochemical treatment, metallographic processing, and microstructural characterization of ASTM A29 steel.*

X-ray diffraction (XRD) analyses were conducted using a Phillips PW 1710 device, with Co $K\alpha_{1,2}$ (λ = 0.179 nm), a step size of 0.01° s^{-1}, and a 2θ scanning range from 0° to 120°. The Vickers microhardness profiles were determined according to ASTM C1327 [18] using a conventional DuraScan 20 G5 hardness tester under two loads 50 and 100 gf and dwell time of 15 s. To assess the brittle behaviour of borided surfaces under indentation, the

qualitative images of indents were categorized using the Vigdorovich–Nashel'skii system [19]. This a commonly used method for evaluating the brittle character of indented materials. According to the Figure 3, this classification ranges from level 0, where no visible damage occurs, to level 5, where extensive cracking is observed around the indentation.

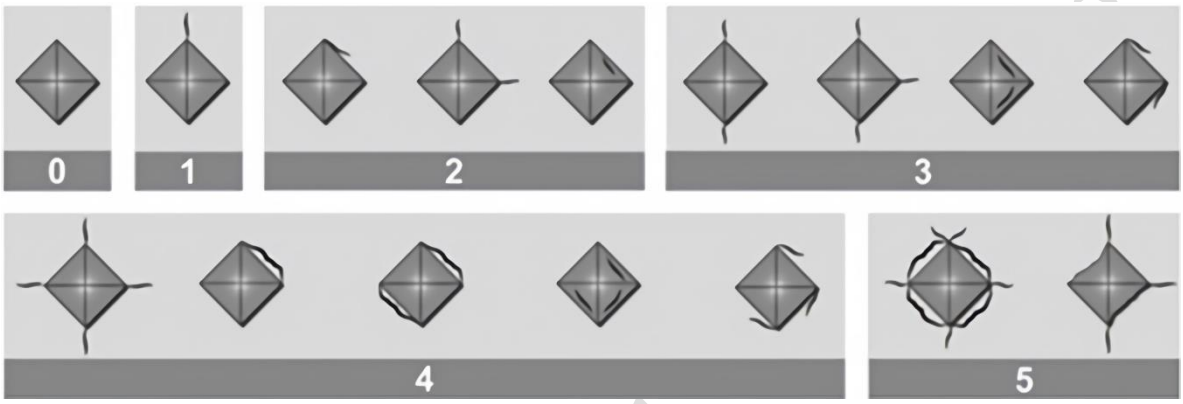

Figure 3. *Classification system used to assess the brittleness of borided surfaces, including indicators of additional damage around the indentation.*

The Young's modulus of Fe_2B layer was determined by nanoindentation using a TTX-NHT tabletop tester (CSM Instruments) equipped with a Berkovich indenter, following the Oliver and Pharr procedure [20]. This method establishes a relationship between the applied force on the diamond tip and the penetration depth, producing load-displacement curves that exhibit elastic-plastic deformation during loading and elastic recovery for unloading. The friction behaviour of ASTM A29 steel samples was assessed using pin-on-disc wear tests, comparing untreated surfaces with the borided ones. The pin-on-disc tests were carried out in dry sliding conditions at ambient temperature using a CSM tribometer with a relative humidity of 40% [21].

2.3 The Taylor expansion model

The Taylor expansion model [11] is employed to evaluate the B diffusion coefficients in Fe_2B layers formed on ASTM A29 steel. In this modelling approach, the distribution

function of B concentration is approximated by a second-order Taylor series expansion in the vicinity of the growing interface, while accounting for the boride incubation time. Figure 4 shows a schematic representation of the B concentration profile together with the corresponding microstructure of the Fe_2B layers developed on ASTM A29 steel.

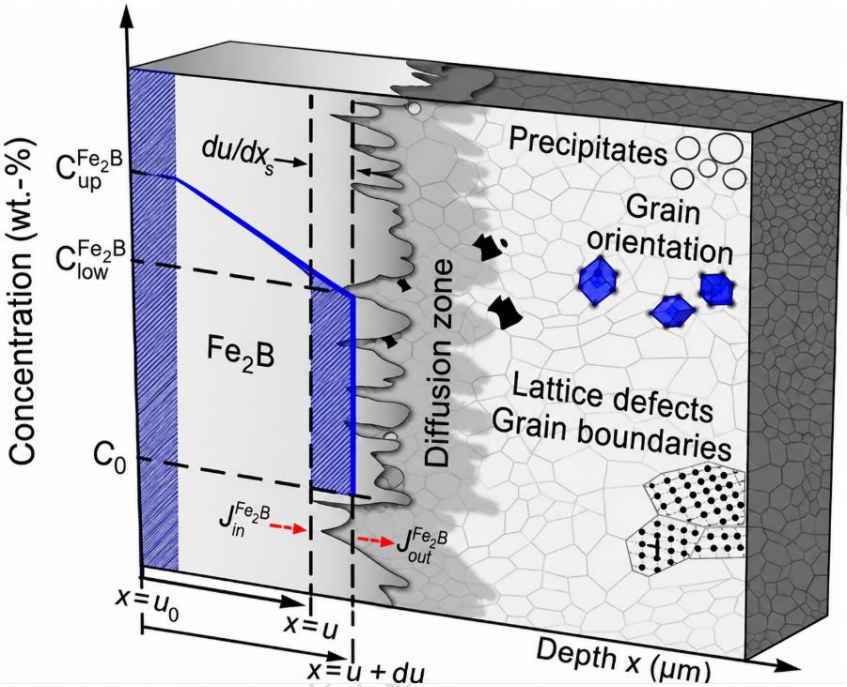

Figure 4. *The generated Fe_2B layer along with the B distribution accross it.*

$C_{up}^{Fe_2B}$ (=9.00 wt.%) is the upper B content in Fe_2B while $C_{low}^{Fe_2B}$ (=8.83 wt.%) is the lower B content in the same phase. u is representative of the Fe_2B layer thickness whose relation is expressed by Equation (4). C_0 denotes the solublity of B atoms inside the substrate which is negligeable ($\approx$0 wt.%) [22].

$$u = k\sqrt{t - t_0} \tag{1}$$

In which the parameter k is representative of parabolic growth constant for Fe_2B, with t_0 the incubation period of Fe_2B layer. The kinetics of this process are governed by the following first-order differential equation:

$$\frac{(C_{up}^{Fe_2B}+C_{low}^{Fe_2B})}{2D_{Fe_2B}}(u\frac{du}{dt})[1+\frac{1}{2D_{Fe_2B}}(u\frac{du}{dt})]=(C_{up}^{Fe_2B}-C_{low}^{Fe_2B}) \quad (2)$$

The analytical solution of Equation (2), analogous to Equation (1), is presented in Equation (3):

$$u=\sqrt{2gD_{Fe_2B}(t-t_0)} \quad (3)$$

with

$$g=-1+\sqrt{1+4\frac{(C_{up}^{Fe_2B}-C_{low}^{Fe_2B})}{(C_{up}^{Fe_2B}+C_{low}^{Fe_2B})}} \quad (4)$$

Ultimately, the B diffusion coefficient in the Fe_2B layer can be obtained, as shown in Equation (5):

$$D_{Fe_2B}=\frac{k^2}{2g} \quad (5)$$

3. Results and discussions

3.1 SEM visualization of the cross-sections of borided ASTM A29 steel samples with EDS analysis.

Figure 5 presents SEM visualisation of the cross-sections of boronized samples for 6 h at different temperatures. The optical images clearly show the formation of dense and continuous Fe_2B layers on the ASTM A29 steel surface, with a less pronounced saw-tooth morphology at the (boride layer/ substrate) interface. The Fe_2B layers exhibit a uniform thickness across all samples, indicating that the boriding process was well controlled. The Fe_2B layer thickness increases with rising temperature after 6 h of treatment, growing from 37.69 ± 5.9 to 137.96 ± 22.6 µm as a result of enhanced boron diffusion. Regardless of the processing parameters, the developed interfaces exhibit an acicular morphology, although it is less pronounced. The needle-like boride morphology, with varying lengths, is particularly evident in Armco iron [23] and low-carbon steels [24], whereas in high-alloy steels [25] it tends to evolve toward a more planar interface.

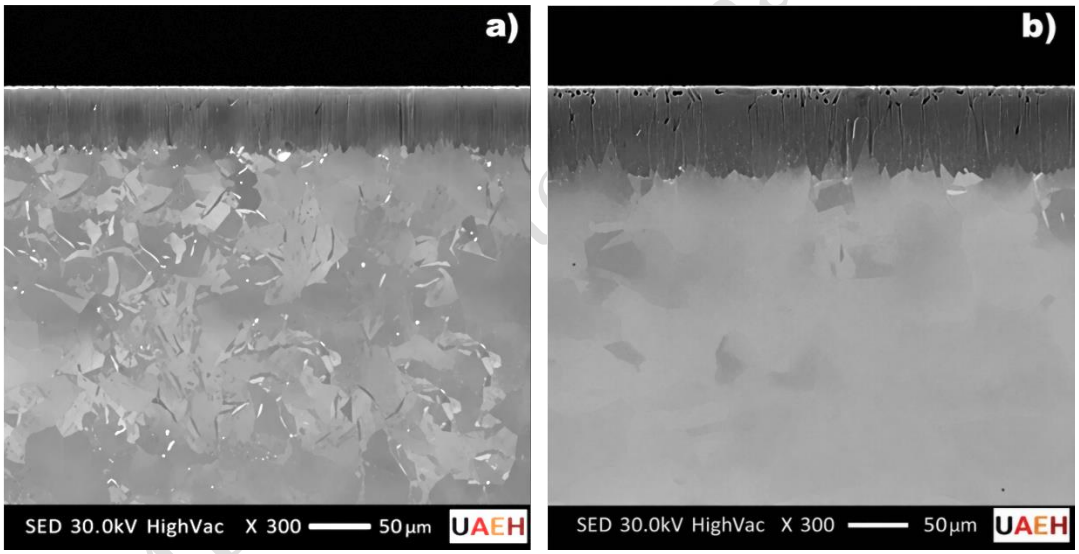

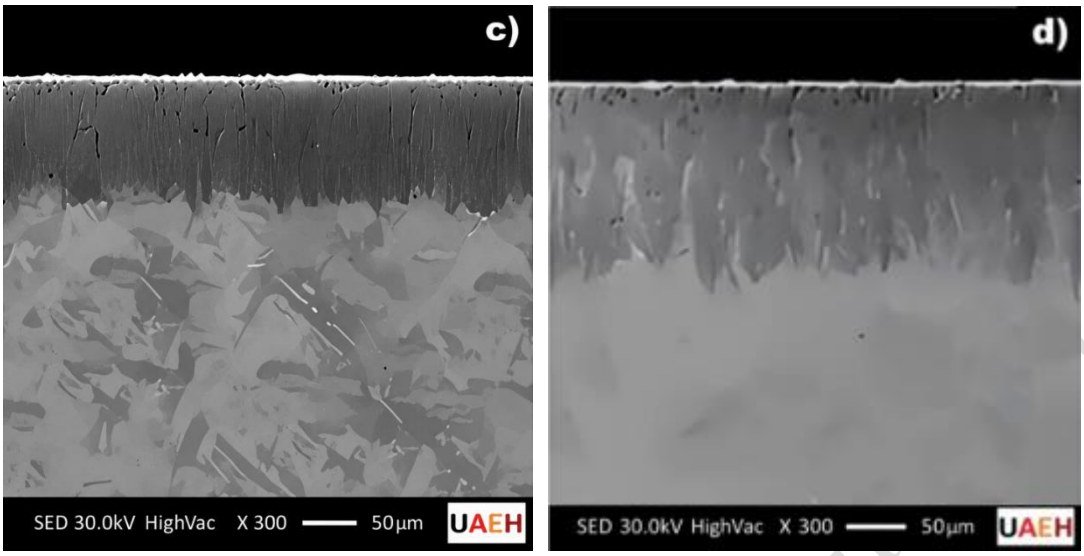

Figure 5. *SEM micrographs showing the Fe_2B layers on the ASTM A29 steel obtained at different temperatures for 6 h: (a) 1123 K, (b) 1173 K, (c) 1223 K, and (d) 1273 K.*

Figure 6 shows SEM micrographs of cross-sections of borided ASTM A29 steel, together with qualitative energy-dispersive spectroscopy (EDS) results. The EDS analyses were performed to identify the characteristic peaks of iron and boron, as well as those of other elements present within the boride layer. In Figure 6a, near the surface region, distinct peaks corresponding to boron and iron are observed. This indicates the reactive diffusion of boron atoms with iron atoms, leading to the formation of the Fe_2B phase when the boron concentration reaches a critical equilibrium value close to its theoretical content in this phase. In contrast, at the interface between the Fe_2B layer and the substrate (Figure 6a), the boron peak is no longer detected due to its extremely low concentration. Consequently, boron is not observed in this region, as its solubility away from the boride layer is negligible. The EDS results show that the Fe_2B layer contains about 8.28 wt.% boron, which is in close agreement with the theoretical composition of this phase. It should be noted that the detection of light elements such as boron requires high-sensitivity instrumentation, typically employing silicon-or lithium-based detectors. Furthermore, the analysis indicated that elements such as Si, C, and Mo do no dissolve in the lattice of Fe_2B phase, whereas Cr and Mn were found to be soluble within the Fe_2B layer, in accordance with previous finding [26]. The obtained results are in qualitative agreement with the

findings reported by Kul et al. [27], who formed a Fe_2B layer on AISI 8620 steel via liquid boronizing. In their work, the elemental analysis indicated a progressive reduction in boron content (wt.%) from the surface towards the steel matrix. They overestimated the B concentration in Fe_2B to approximately 20 wt.% using EDS analysis, whereas in our study the corresponding concentration was 8.28 wt.%.

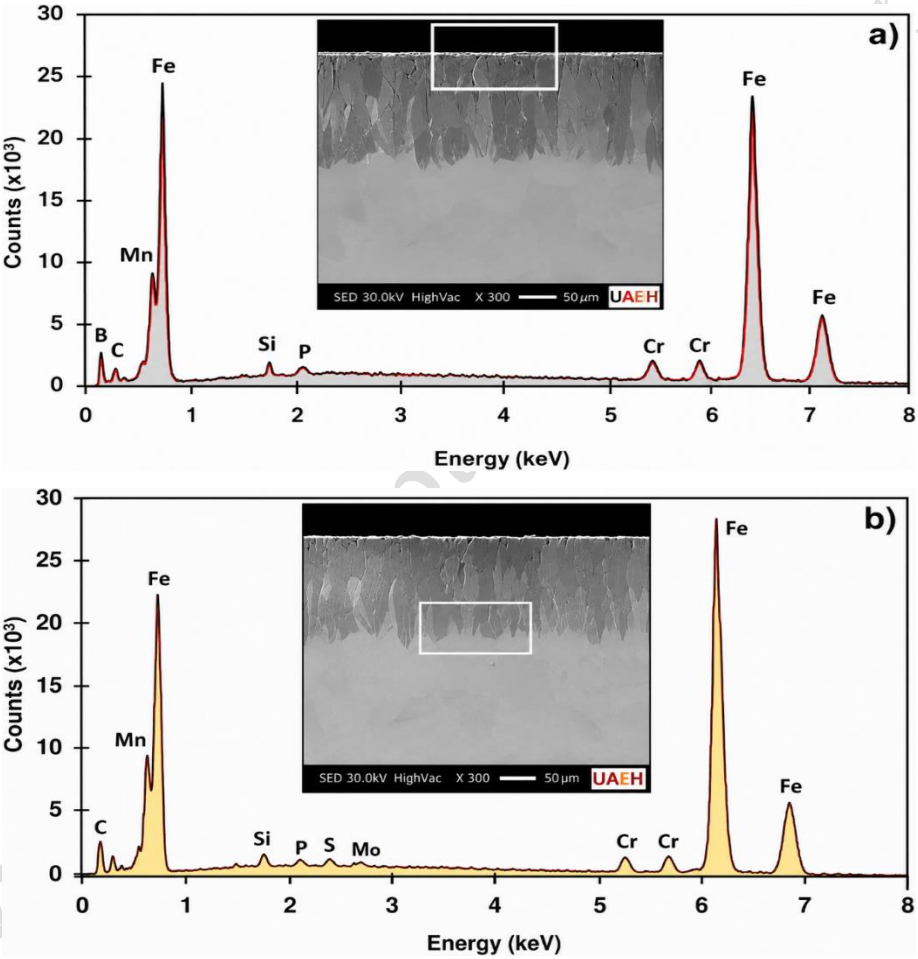

Figure 6. *SEM images of cross-sections of boride layers obtained at 1273 K for 8 h along with the EDS analyses in two distinct locations: (a) near the top surface, (b) at the (boride layer/substrate) interface.*

3.2 XRD analysis

Figure 7 shows the diffraction patterns of samples treated at 1273 K for 4, 6, and 8 h, illustrating the progressive development of the boride layer with increasing treatment duration. The observed diffraction peaks correspond exclusively to the Fe_2B phase, with no secondary phases detected. In addtion, the obtained diffracting peaks pertaining to the Fe_2B phase vary in intensity depending upon the treatment times at 1273 K. According to ICDD reference 00-036-1332, the diffraction peaks observed near 50° correspond to the most intense reflections of the Fe_2B phase. They are consistently present in all diffraction patterns, thereby confirming the formation of the Fe_2B phase. The amount of boron atoms in the powders mixture was therefore sufficient to give rise to the Fe_2B phase after reactive diffusion with iron atoms. Sánchez-Fuentes et al. [26] used the commercial reused boron paste to treat the AISI 9254 steel at temperatures ranging from 1173 to 1273 K. XRD analyses revealed the formation of Fe_2B layer, along with secondary boride precipitates such as MnB and CrB. These findings are in line with the present study. However, in our work, secondary phases were not detected within the Fe_2B layer formed on the treated steel, due to differences in the proportion of alloying elements.

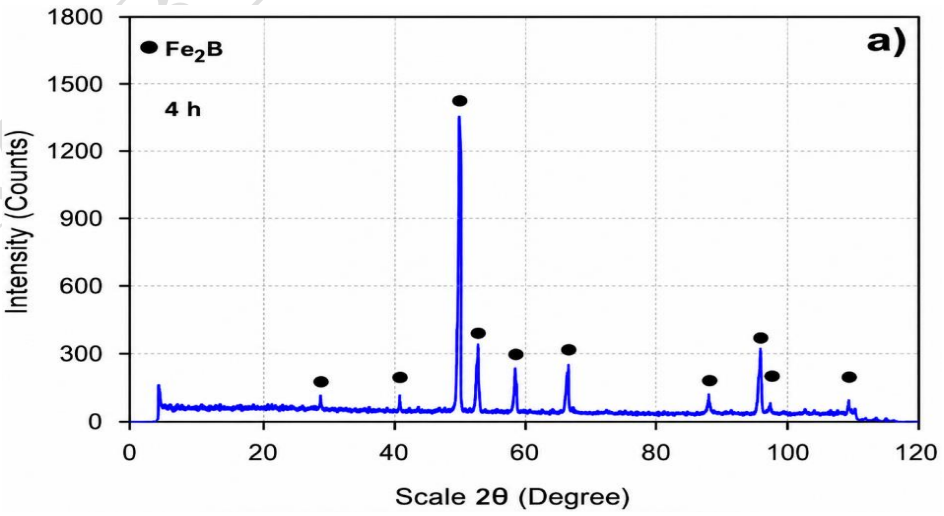

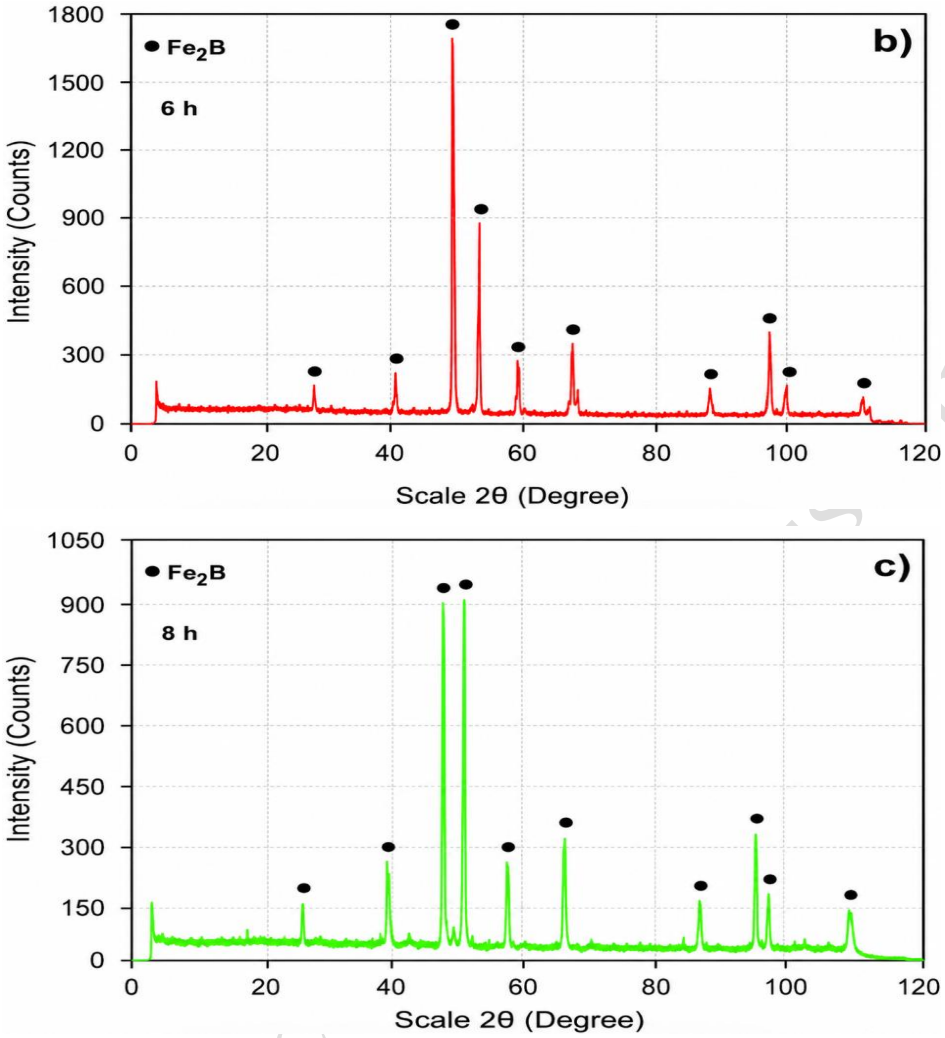

Figure 7. *XRD diffractograms of borided surfaces of ASTM A 29 steel at 1273 K for different treatment times: (a) 4 h, (b) 6 h, and (c) 8 h.*

3.3 Microhardness mesurements

Figure 8 shows the Vickers indents on SEM images of the cross-sections of boride layers obtained at 1223 K for 6 h and at 1273 K for 4 h, respectively. It is seen that the measured diagonals of the Vickers indents vary across the boride layer. Based on the XRD analyses, a monophased layer was formed, and the Fe_2B phase is known to exhibit very high hardness values, typically ranging from 1800 to 2000 HV [28, 29]. The analysis of the borided

samples confirms that the surface exhibits extremely high hardness as a result of the Fe_2B layer formation on the steel substrate.

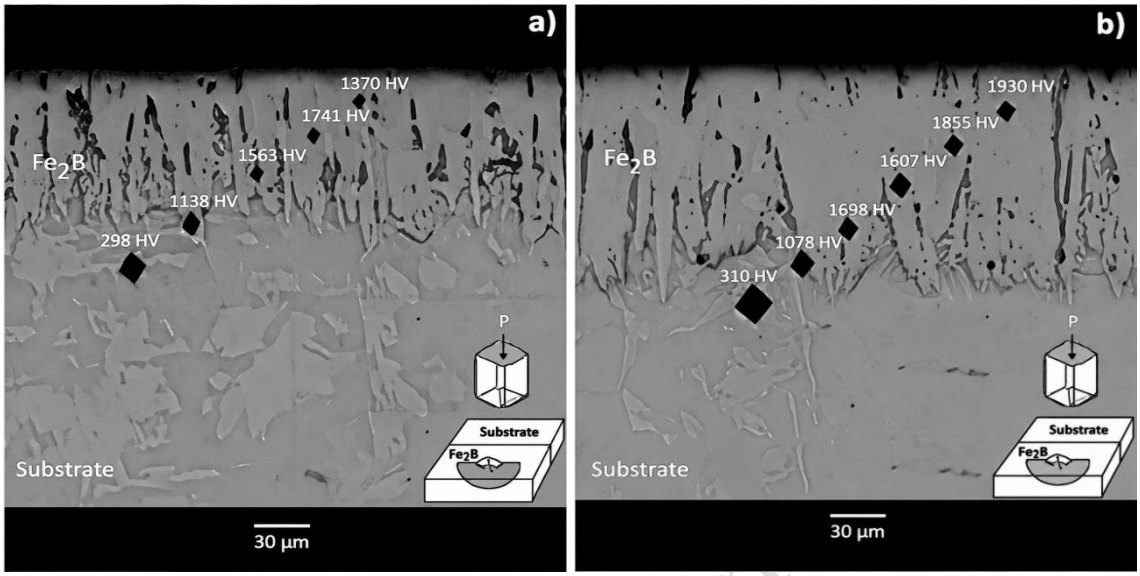

Figure 8. *Optical images showing the Vickers indents along the boride layers for two different loads and processing parameters : (a) 6 h at 1223 K under a load of 50 gf, and (b) 4 h at 1273 K under a load of 100 gf.*

As illustrated in Figures 8a and 8b, the samples exhibited surface hardness values of 1870 $HV_{0.05}$ and 1930 $HV_{0.10}$, respectively. These results indicate that higher boriding temperature significantly improves the coating hardness. By comparison, the substrate showed an average hardness of 304 $HV_{0.10}$, demonstrating that boriding improves the surface hardness of ASTM A29 steel by a factor of 6.25. It is reported that, several factors can affect the surface hardness of Fe_2B layers, namely residual thermal stresses, boriding conditions and time, the chemical composition of the substrate, and the anisotropy properties of the coating [29, 30]. Based on previously reported literature results, Li et al. [31] boronized the 18CrNiMo7-6 steel under vacuum condition employing a powder mixture with : (10 wt.% B_4C, 10 wt.% KBF_4, and 80 wt.% SiC). The resulting boride layers exhibited a biphasic microstructure (FeB and Fe_2B) after treatment at 1273 K for 1, 2, and 4 h. The measured average microhardness values of the FeB and Fe_2B layers were 1440 $HV_{0.05}$ and 1050 $HV_{0.05}$, respectively. Notably, the Vickers microhardness of the Fe_2B layer

reported by Y. Li et al. [31] was lower than the value obtained in the present study. It is widely recognized that the Vickers hardness of FeB and Fe_2B layers is greatly affected by the applied treatment parameters [32,33]. To evaluate the brittle behaviour of the coating after indentation, the resulting impressions were classified according to the Vigdorovich–Nashel'skii scheme [19], which is widely applied to brittle materials.

As depicted in Figure 3, the damage levels range from 0 (no observable damage) to 5 (severe cracking around the indent). Figure 9 shows the indentation responses of borided surfaces treated at 1273 K for 4 h under two applied loads of 50 gf and 100 gf. The micrographs reveal that higher applied loads result in increased surface damage, characterized by more pronounced cracking and material deformation, indicative of the brittle behaviour of the Fe_2B layer. As shown in Figure 9a, crack initiation primarily occurs at the indentation corners. In contrast, Figure 9b reveals that cracking is concentrated along or near the indentation perimeter, forming a characteristic semicircular pattern. This behaviour is associated with the pronounced anisotropy of the Fe_2B phase. Its body-centered tetragonal crystal structure possesses preferential cleavage planes that induce volumetric expansion and generate circumferential tensile stresses, which facilitate the formation and propagation of curved cracks, rather than the linear cracks typically observed in other ceramic phases such as FeB [34].

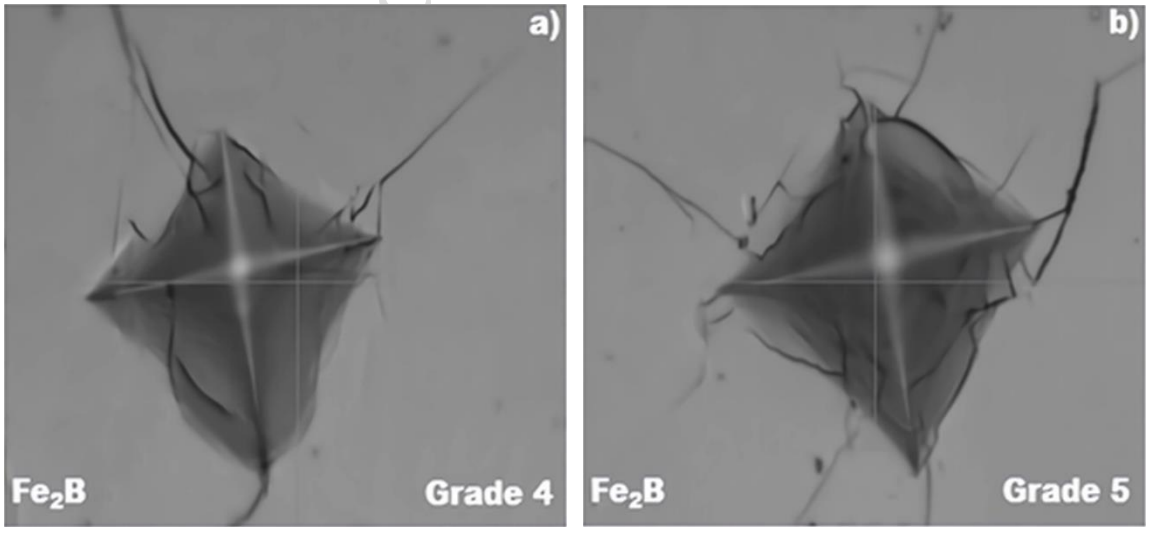

Figure 9. *Behaviour of Fe_2B layers formed on ASTM A29 steel (1273 K for 4 h) under two applied loads using a Vickers indenter: (a) 50 gf and (b) 100 gf.*

Furthermore, the development of semicircular crack patterns in tetragonal ceramics is strongly affected by crystallographic orientation. Chevalier et al. [35] demonstrated that crack propagation preferentially follows crystallographic directions perpendicular to the transformation plane, resulting in a semicircular crack network around the indentation.
It is observed that the processing parameters directly affects the thickness, morphology, and mechanical response of the Fe_2B layer. Higher temperatures and longer treatment times promote the formation of thicker boride layers with increased hardness due to enhanced boron diffusion kinetics. However, these conditions also contribute to higher residual stresses and increased crack sensitivity during indentation testing. In the present work, the samples borided at 1273 K for 4 h exhibited brittleness grades 4 and 5 under applied loads of 50 gf and 100 gf, respectively. The transition from grade 4 to grade 5 indicates that increasing the applied load intensifies crack nucleation and propagation around the indentation site. This behaviour is associated with the intrinsic brittleness of the Fe_2B phase and its anisotropic tetragonal crystal structure, which promotes preferential crack propagation along specific crystallographic directions.

3.4 Estimation of the elastic modulus of Fe_2B layers via nanoindentation testing

SEM images of the borided steels, presented in Figure 10, show the indentations obtained at 1223 K for 6 h (Figure 10a) and 1273 K for 4 h (Figure 10b). In Figure 10a, the nanohardness and elastic modulus were measured at 21.75 GPa (H_{IT}) and 360 GPa (E_{IT}), respectively. For Figure 10b, the corresponding values were 21.98 GPa (H_{IT}) and 376 GPa (E_{IT}), in good agreement with previously reported data for the Fe_2B phase [34].

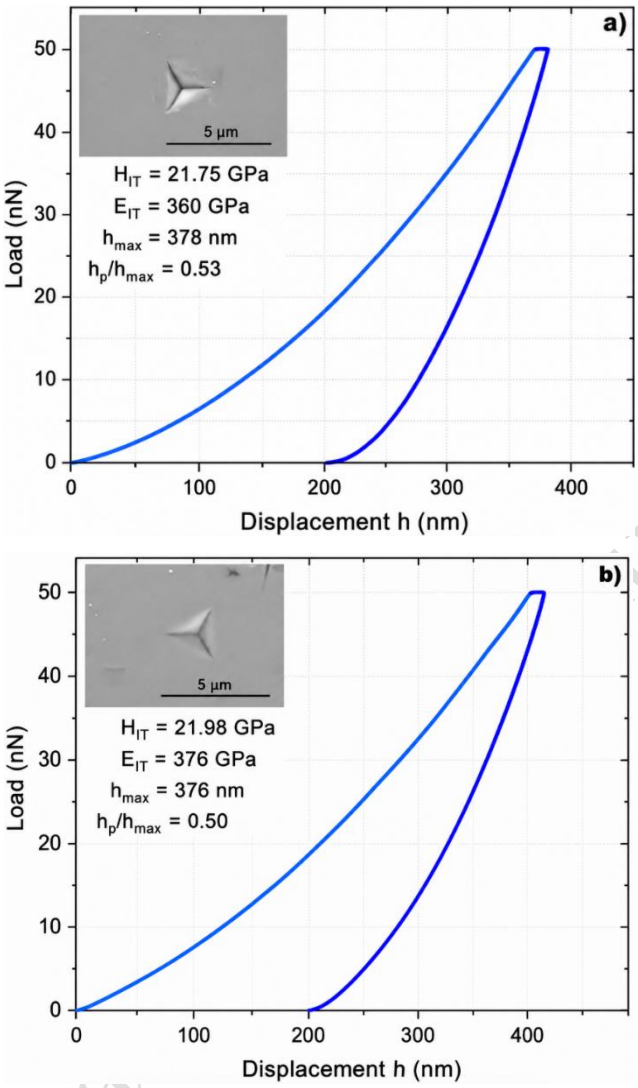

Figure 10. *SEM images of indents and nanoindentation curves for two processing parameters (a) steel borided at 1223 K for 6 h and (b) steel borided at 1273 K for 4 h.*

Kulka et al. [36] determined the elastic moduli of the iron borides (FeB and Fe_2B) as well as their nanohardness in pack-boronized X165CrV12 steel using an applied load of 50 mN. They reported an average elastic modulus of 339.75 ± 17.44 GPa, together with a corresponding nanohardness value of 17.45 ± 1.20 GPa. Reported values for the elastic modulus of iron borides vary from one study to another in the literature. For instance,

Kulka et al. [37] evaluated the elastic modulus of Fe_2B layers formed on Armco iron by gas boriding. Two types of iron borides were produced on the surface at 1193 K for 3 h. Using a Berkovich diamond nanoindenter under a load of 50 mN, they measured an elastic modulus of 252.96 ± 15.57 GPa and a nanohardness of 17.42 ± 0.80 GPa. The higher load used in their nanoindentation tests likely accounts for the differences in elastic modulus compared to the results obtained in the present study. In another work, Rodríguez-Castro et al.[38] performed mechanical characterization of borided AISI D2 steel using the Berkovich nanoindentation technique. They reported that the elastic modulus of the Fe_2B layers, measured at a constant load of 250 mN, ranged from 242 to 290 GPa, which differs from the values obtained in the present study. This discrepancy is likely due to the lower applied load of 55 mN and differences in other processing parameters.

3.5 Tribological performance evaluation of Fe_2B layer

The frictional performance of ASTM A29 steel was evaluated using the pin-on-disc wear tests, comparing untreated steel with borided one. Figure 11 shows the variation of the friction coefficient as a function of sliding distance under dry conditions for both untreated and borided steels. The results reveal a substantial decrease in friction after the boriding treatment. In particular, boriding at 1273 K for 8 h resulted in the formation of a hard boride layer, which lowered the average friction coefficient to approximately 0.25–0.29, whereas the untreated steel exhibited higher values in the range of 0.60–0.62. Comparable reductions in friction due to boriding have also been documented in previous studies, irrespective of the processing parameters employed [39].

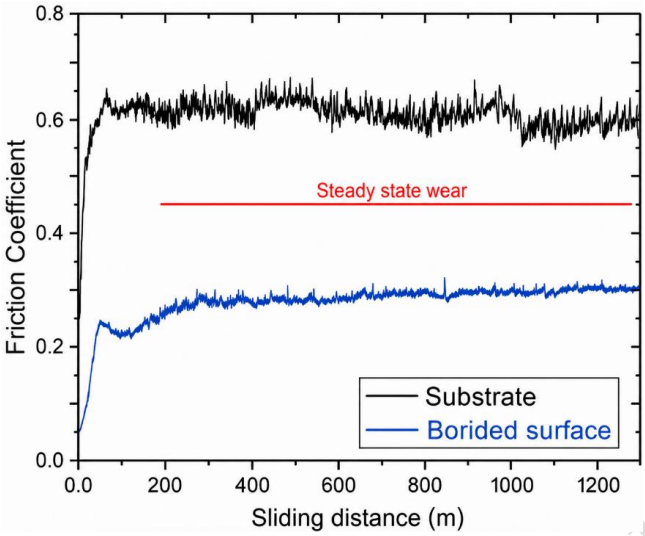

Figure 11. *Evolution of the friction coefficient as a function of sliding distance for two ASTM A29 steel surfaces: borided (1273 K for 8 h) and unborided.*

Figure 12 presents the wear scar profiles versus the sliding distance for both borided and untreated steels after the wear tests. As illustrated, the borided ASTM A29 steel shows a markedly lower wear rate compared to the untreated substrate. This difference is particularly manifest for the steel treated at 1273 K for 8 h, which produced the thickest boride layer. The untreated steel exhibits severe wear, characterized by a wide and deep wear track, whereas the borided steel displays a significantly narrower and shallower groove, highlighting the improved wear resistance imparted by the Fe_2B layer during dry sliding. This improvement can be attributed to its capability to sustain applied loads and more effectively distribute deformation across the contact surface. These results align with previous studies in the literature [40]. In another study, the wear performance of borided AISI 316L steel was evaluated in detail by Hernández-Sánchez et al. [41]. Their results indicated that the selected processing parameters had a significant influence on the wear performance of the borided layers. The lowest friction coefficient (= 0.3) was obtained for the sample borided at 950°C for 6 h, whereas the untreated steel had a higher value of 0.8. This substantial reduction in friction was ascribed to the formation of H_3BO_3, which acts as an effective solid lubricant on the boronized surface. In addition, the results showed that a single-phase Fe_2B layer had greater resistance to wear than the bilayer (FeB + Fe_2B).

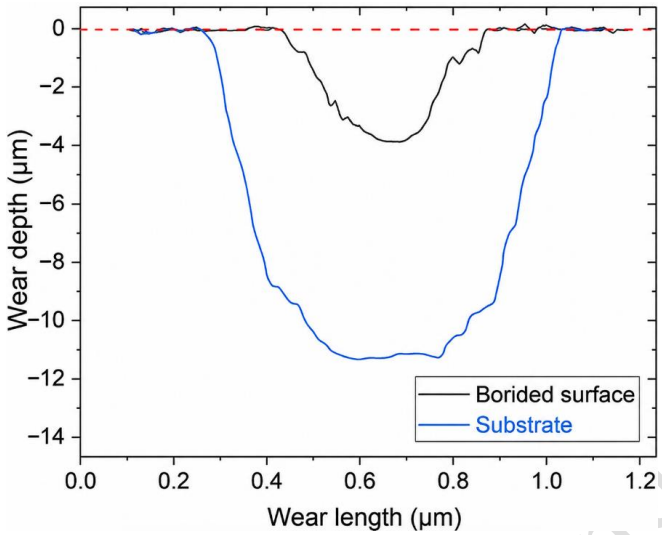

Figure 12. *Wear scar profiles of untreated and surface-hardened ASTM A29 steel after boriding at 1273 K for 8 h..*

Based on the quantitative interpretation of the Vigdorovich–Nashel'skii classification, it is evident that the boriding parameters strongly affect the balance between hardness and fracture resistance. Although higher boriding temperatures improve tribological performance through the formation of thicker Fe_2B layers with superior wear resistance, excessive brittleness may reduce coating reliability under severe impact or cyclic loading conditions. Therefore, optimization of the boriding parameters is essential to obtain coatings with an appropriate balance between hardness, wear resistance, and crack tolerance during service. Regarding other reported works on borided iron-based alloys, Lopez-Leyva et al. [42] investigated the combined effects of boriding, interrupted austempering, and cryogenic treatment on the brittleness behaviour of 8 wt.% Cr alloyed steel. Their results revealed that the brittleness grades were strongly correlated with the hardness values of the treated material. Furthermore, the combined boriding and post-treatment processes markedly influenced both the wear performance and brittleness characteristics of the steel. The highest wear resistance was achieved in the borided, interrupted austempered, and cryogenically treated samples, which was attributed to the transformation of the bilayer (FeB + Fe_2B) into a single Fe_2B layer. In another study, Tlili

et al. [43] applied the boriding process to 13Cr5Ni2Mo steel at 950 °C for 4 h. Their study revealed the formation of a bilayer (FeB + Fe_2B), together with metallic boride precipitates. After boriding, the surface hardness increased significantly, attaining approximately 2160 $HV_{0.05}$. Nanoindentation measurements revealed that the Young's modulus values were about 26.367 GPa for FeB and 24.294 GPa for Fe_2B. In addition, the boriding process considerably enhanced the wear resistance of 13Cr5Ni2Mo steel, with the improvement depending on the applied normal load. The wear performance was reported to increase by nearly 6 to 13 times compared with the untreated substrate. Ayvaz [44] pack-borided the AISI 1050 steel at 875 °C for treatment durations of 2, 4, and 6 h. Their results revealed that the dominant phase formed within the boride layer was Fe_2B. The treated samples exhibited a maximum surface hardness of 1543.8 $HV_{0.1}$. In addition, the specific wear loss was significantly reduced by a factor of approximately 24 compared with the untreated substrate, indicating a significant enhancement in wear resistance after boriding. Concerning the boriding of non-ferrous alloys, Türkmen et al. [45] investigated the influence of boronizing parameters on the mechanical and tribological properties of Monel K-500. Their results revealed that the boronized alloy exhibited an approximately tenfold increase in surface hardness and a twenty-fourfold enhancement in wear resistance compared with the untreated substrate. In another study, Kara and Pürçek [46] studied the influence of boride coatings on the wear behaviour of biomedical grade Ti–45Nb alloy. The study focused on the influence of boriding treatment on the tribological performance, wear mechanisms, and surface degradation of the alloy under dry sliding conditions. They reported that the formation of hard boride layers significantly improved the wear resistance of Ti–45Nb alloy by reducing material loss, surface damage, and friction-related deterioration compared with the untreated substrate. Selective Laser Melting was employed by Attar et al. [47] to fabricate Ti and Ti–TiB composite materials, whose nanoindentation and wear properties were subsequently evaluated. The study examined the effect of TiB reinforcement on the microstructure, nanohardness, elastic modulus, and tribological behaviour of the produced composites. They reported that the incorporation of TiB phase significantly enhanced the tribological performance and nanomechanical properties of the titanium matrix, while simultaneously reducing material loss and friction during sliding wear tests.

3.6 Exploitation of the Taylor expansion model

The Taylor expansion model [11] was employed to evaluate the boron diffusivity in Fe_2B over the temperature range 1123–1273 K. Figure 13 illustrates the evolution of the square of the layer thickness as a function of treatment time within the considered temperature range. It is noted that characteristic incubation periods have similar values across the investigated temperature range.

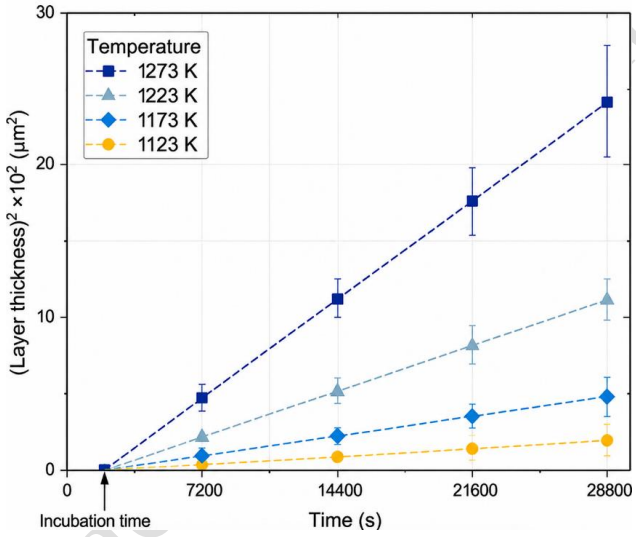

Figure 13. *Kinetic analysis of Fe_2B layer growth over time.*

Table 2 gives the experimental k values from the kinetic analysis and the corresponding incubation times, independent of temperature.

Table 2. *Experimental k values with the incubation times in the temperature range 1123-1273 K.*

T (K)	k (µm·s$^{-0.5}$)	t_0 (s)
1123	0.2688	1950.1

1173	0.4241	1950.3
1223	0.6446	1949.7
1273	0.9841	1949.2

In Table 3, are included the assessed B diffusion coefficients in Fe_2B for a constant dimensionless parameter that is independent of temperature.

Table 3. *Assessed B diffusion coefficients in Fe_2B with the Taylor expansion model.*

T (K)	D_{Fe_2B} ($\times 10^{-12}$ m^2 s^{-1})
1123	1.91
1173	4.76
1223	10.99
1273	25.63

By considering the linear fitting of the temperature dependence of boron diffusivity through the Fe_2B layers in accordance with the Arrhenius relationship [48], Equation (6) was derived as follows:

$$D_{Fe_2B} = 6.48 \times 10^{-3} exp\left(-\frac{205\, kJ\ mol^{-1}}{RT}\right) \quad (6)$$

Where T denotes the temperature in Kelvin and R = 8.314 J $mol^{-1} \cdot K^{-1}$ the universal gas constant.

Table 4 list the published values of B activation energies obtained on some borided steels along with the value found in the present study [13, 32, 49-55]. The differences in activation energy reported in Table 4 are strongly influenced by several intrinsic factors governing the boriding kinetics, including: (i) the chemical composition of the substrate, particularly the concentration of alloying elements such as Cr, Mn, Mo, and Si, which may affect boron mobility and the formation of alloy borides; (ii) the activity and composition of the boron source, since different powder mixtures and reactive media modify the concentration of active boron species available at the steel surface; (iii) the boriding technique employed (powder-pack, plasma, electrochemical, Cathodic Reduction and Thermal Diffusion (CRTD), boro-sintering, etc.), which changes the diffusion mechanism and the kinetics of boron transfer; and (iv) the dominant diffusion paths, including lattice diffusion, grain-boundary diffusion, and defect-assisted diffusion mechanisms. In addition, differences in the activation energy may arise from the methodology used for its evaluation, either through empirical relations based on the classical parabolic law [49,51–53] or through diffusion models [11,13,16,32,54,55]. For example, Castillo-Vela et al. [13] recently patented a surface modification process, abbreviated as PDCPB, for boronizing the AISI 1018 and AISI 4140 steels. Their results revealed lower boron activation energy values, which were attributed to the influence of electromigration on boron diffusion, leading to enhanced diffusion kinetics. The 4Cr5MoSiV1 steel was borided by Delai et al. [32] with 5 wt.% B_4C, 4 wt.% KBF_4, 5 wt.% C, and 88 wt.% SiC. This powders mixture gave rise to the FeB and Fe_2B layers. The activation energies calculated using the error-function model were 205.25 and 170.91 $kJ \cdot mol^{-1}$ for FeB and Fe_2B, respectively. The activation energy obtained for the Fe_2B phase was lower than that reported in the present work, which can be attributed to differences in powder mixture composition and processing parameters. Gunes et al. [49] plasma- paste borided the surfaces of AISI 8620 steels with 100 wt.% borax as well as borax-based mixtures containing B_4C or SiC in different proportions. Their kinetic analysis yielded activation energy values between 99.77 and 108.24 $kJ \cdot mol^{-1}$. The lowest activation energy was obtained for the paste containing 100 wt.% borax. This fact was ascribed to plasma activation, which enhances the release of active boron ions responsible for iron boride formation. In another study, Kartal et al. [50] carried out the boronizing of AISI T1 steel using an environmentally friendly technique

known as cathodic reduction and thermal diffusion (CRTD). The activation energy determined in this case was 179 kJ·mol^{-1} for AISI T1 steel. The activation energy obtained in the present study is lower than the reported value, which can be ascribed to differences in the kinetics of the chemical or electrochemical reactions involved. Moreover, this process offers the advantage of reducing the treatment time and promoting subsequent phase homogenization, leading to the formation of a single Fe_2B layer. Kayali [51] pack-borided the AISI 304L steel using an Ekabor powder mixture in the temperature range 1123–1223 K. This treatment led to the formation of FeB and Fe_2B layers, along with metal boride precipitates, with an estimated activation energy of 222.81 kJ·mol^{-1}. This value is higher than that obtained in the current work, since the chemical compositions of the two steels (AISI 304L and ASTM A29) are not identical. Ayvaz et al. [52] employed the boro-sintering process on AISI 316 steel fabricated by powder metallurgy. They obtained an activation energy of 190.29 kJ·mol^{-1} for this steel. In addition, it was shown that the sintering temperature and processing parameters strongly affected the porosity level of the densified AISI 316 steel substrates. During boro-sintering, densification was governed by competing mechanisms, including surface diffusion, grain-boundary diffusion at the formed interfaces, and diffusion associated with plastic deformation. Mourad et al. [53] applied the electrochemical boriding to the AISI H13 steel. This thermochemical treatment was performed in a molten borax bath composed of 22.5 wt.% ferroboron, 70 wt.% borax, and 7.5 wt.% NH_4Cl, within the temperature range 1123–1323 K, under an applied current density of 200 mA·cm^{-2}. The process resulted in the formation of a bilayer (FeB+ Fe_2B) with an activation energy of 168.4 kJ·mol^{-1} different from the current work. This difference can be attributed to the nature and kinetics of the electrochemical reactions involved in electrochemical boriding compared with powder-pack boriding.

Table 4. *Comparative analysis of the differences in activation energy values*

Steel	Type of	Temperature	Activation energy	The approach	Refs.

	boriding	interval (K)	($kJ\ mol^{-1}$)	used	
AISI 8620	Plasma paste	973-1073	99.77-108.24 ($FeB + Fe_2B$)	Parabolic growth law	[49]
AISI 1018	PDCPB	1073-1173	148.2 ±8.2 (Fe_2B)	MDC model	[13]
AISI 4140	PDCPB	1073-1173	155.2 ±8.1 (Fe_2B)	MDC model	[13]
AISI T1	CRTD	1123-1323	179 ($FeB + Fe_2B$)	Parabolic growth law	[50]
AISI 304L	Powder	1123-1223	222.81 ($FeB+ Fe_2B$)	Parabolic growth law	[51]
4Cr5MoSiV1	Powder	1123-1253	205.25 (FeB) 170.91 (Fe_2B)	Transient diffusion model	[32]
AISI 316	Boro-sintering	1173-1273	168.4 ($FeB+ Fe_2B$)	Parabolic growth law	[52]
AISI H13	Electro-chemical	1123-1323	168.4 ($FeB+ Fe_2B$)	Parabolic growth law	[53]
AISI H13	Powder	1123-1273	240.37 (FeB) 232.62 (Fe_2B)	Modified diffusion model	[54]
AISI 1045	Powder	1123-1273	180 (Fe_2B)	Transient diffusion model	[55]
ASTM A29	Powder	1123-1273	205 (Fe_2B)	Taylor expansion model	This work

Figure 14 presents SEM micrographs of the cross-sections of boronized ASTM A29 steel processed under four additional boronizing conditions. The proposed model was experimentally validated by using four additional boriding conditions: (1173 K for 9 h,

1223 K for 3 and 4.5 h as well as 1273 K for 5 h) The results shown in Table 5 indicate that the model reproduces the experimental data with good accuracy.

Table 5. *Experimental verification of the Taylor expansion model using four boriding conditions.*

Boriding conditions	Experimental Fe_2B layer thickness (μm)	Predicted Fe_2B layer thickness (μm)
1173 K for 9.0 h	72.41 ± 10.3	74.40
1223 K for 3.0 h	60.65 ± 9.85	60.52
1223 K for 4.5 h	75.06 ± 11.55	76.92
1273 K for 5.0 h	120.8 ± 19.89	123.30

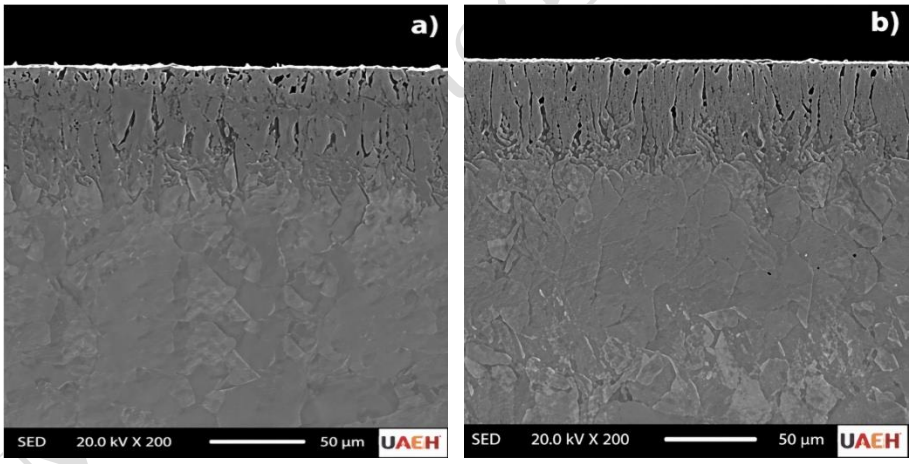

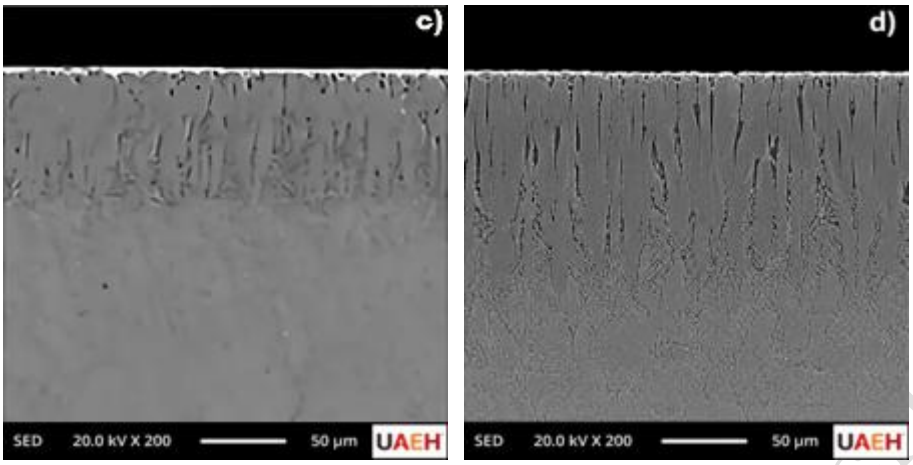

Figure 14. *SEM micrographs of cross-section of borided ASTM A29 steels for 4 additional processing parameters: (a) 1173 K for 9 h, (b) 1223 K for 3 h, (c) 1223 K for 4.5 h and (d) 1273 K for 5 h.*

4. Conclusions

In the present study, ASTM A29 steel was surface-hardened by boriding which was carried out at temperatures between 1123 and 1273 K, with holding times of up to 8 h. The main findings of this investigation are the following:

1. The boronized layers on ASTMA29 steel was compact and monophased with a saw tothed shape having layer thickness ranged from 19.48 ± 2.2 to 161.27 ± 26.2 µm.

2. The XRD analysis identified a monolayer composed of Fe_2B phase without secondary phases for the selected processing parameters.

3. The highest surface hardness values measured using the Vickers indenter were 1870 $HV_{0.05}$ and 1930 $HV_{0.10}$, achieved for the steels borided at 1223 K for 6 h and 1273 K for 4 h, respectively, at a depth of approximately 10 µm from the surface. In contrast, the Vickers hardness of the substrate had a value of 304 $HV_{0.10}$.

4. The influence of the applied Vickers load on the brittle behaviour of the Fe_2B layer formed at 1273 K for 4 h was examined. At a load of 50 gf, the damage was relatively limited, with cracks initiating at the corners of the indentation; this damage was classified as grade 4 as per the Vigdorovich–Nashel'skii criterion. When the load was increased to

100 gf, the indentation damage became more pronounced, with crack propagation exhibiting a semicircular pattern, also categorized as grade 5.

5. During sliding wear tests, the friction coefficient of the steel borided at 1273 K for 8 h ranged between 0.25 and 0.29, whereas the untreated steel exhibited higher values between 0.60 and 0.62. Consequently, the Fe_2B layer contributed to the improved wear resistance of ASTM A29 steel.

6. Based on nanoindentation measurements, the elastic modulus of the Fe_2B phase was found to be 360 and 376 GPa for the samples borided at 1223 K for 6 h and 1273 K for 4 h, respectively. The determined nanohardness values were 21.75 and 21.98 GPa, respectively. These results are in good agreement with those reported in the literature for an applied load of 50 mN.

7. The B activation energy in Fe_2B was determined to be 205 $kJ \cdot mol^{-1}$ for the ASTM A29 steel. The TE model was validated at 1223 K for 3 h and 4.5 h, at 1173 K for 9 h, and at 1273 K during 5 h.The experimental measurements agreed with its predictions

8. Lastly, the Taylor expansion model can also be extended to other diffusion-controlled processes.

Research funding: The work described in this paper was supported by a grant of PRODEP and CONAHCyT México (National Council of Humanities, Science and Technology).

Author Contributions

Visualization, Software and Methodology - original draft, Data curation, Formal analysis, Investigation, M. Ortiz-Domínguez ; Writing – review & editing, Software and Methodology, M. Keddam.

Data Availability Statement

Data will be made available on request.

Conflicts of Interest

The authors declare no conflict of interest.

References

[1] E. Medvedovski, M. Antonov, Erosion studies of the iron boride coatings for protection of tubing components in oil production, mineral processing and engineering applications, Wear, 452-453 (2020) 203277. https://doi.org/10.1016/j.wear.2020.203277

[2] J. Martínez-Trinidad, R. Márquez-Cortés, L. A. Moreno-Pacheco, F. Alonso-Cruz, W.D. Wong-Ángel, R. A. García-León, Effect of the impact angles on the erosion wear resistance of borided AISI 4140 steel, Results Eng., 26 (2025) 104962, https://doi.org/10.1016/j.rineng.2025.104962

[3] J. Di, S. S. Wang, L. Zhang, L. X. Cai, Y. H. Xie, Study on the erosion characteristics of boride coatings by finite element analysis, Surf. Coat. Technol., 333 (2018) 115-124. https://doi.org/10.1016/j.surfcoat.2017.10.042

[4] R. J. K. Wood, L. Ping, Coatings and Surface Modification of Alloys for Tribo-Corrosion Applications, Coatings, 14 (1) (2024) 99. https://doi.org/10.3390/coatings14010099

[5] M. Woydt, The importance of tribology for reducing CO2 emissions and for sustainability, Wear, 474 (2021) 203768. https://doi.org/10.1016/j.wear.2021.203768

[6] K. Holmberg, and A. Erdemir, The impact of tribology on energy use and CO2 emission globally and in combustion engine and electric cars, Tribol. Int., 135 (2019) 389-396. https://doi.org/10.1016/j.triboint.2019.03.024

[7] K. Holmberg, and A, Erdemir, Influence of tribology on global energy consumption, costs and emissions, Friction, 5 (2017) 263-284. https://doi.org/10.1007/s40544-017-0183-5

[8] E. Medvedovski, J. Jiang, and M. Robertson, Tribological properties of the boride-based thermal diffusion coatings, Adv. Appl. Ceram., 113 (7) (2014) 427-437. https://doi.org/10.1179/1743676114Y.0000000175

[9] L. Sánchez Fuentes, N. López Perrusquia, M. C. Elías Espinosa, D. V. Melo Máximo, T. de la Mora Ramírez, V. H. Olmos Domínguez, M. A. Doñu Ruiz, Adhesion Characterization on AISI 9254 steel boriding, Microsc.Microanal., 30 (1) (2024) 1273–1275. https://doi.org/10.1093/mam/ozae044.629

[10] I. Campos-Silva, M. Ortiz-Domínguez, C. VillaVelázquez, R. Escobar, and N. López, Growth kinetics of boride layers: a modified approach, Defect Diff. Forum, 272 (2008) 79-86. https:// doi.org/10.4028/www.scientific.net/DDF.272.79

[11] M. Keddam, P. Orihel, P. Jurci, M. Kusy, Characterization of Boride Layers on S235 Steel and Calculation of Activation Energy Using Taylor Expansion Model, Coatings, 15 (5) (2025) 579. https://doi.org/10.3390/coatings15050579

[12] R. D. Ramdan, T. Takaki, K. Yashiro, and Y. Tomita, The effects of structure orientation on the growth of Fe_2B boride by multi-phase field simulation, Mater. Trans., 51 (1) (2010) 62-67. https://doi.org/10.2320/matertrans.M2009227

[13] L. E. Castillo-Vela, I. Mejía-Caballero, J. L. Rosales-Lopez, M. Olivares-Luna, A. Contreras-Hernández, M. Keddam, I. Campos-Silva, The influence of a pulsed-DC field on

the growth of the Fe_2B layer and the electrical behavior of the boriding media, Vacuum, 210 (2023) 111846. https://doi.org/10.1016/j.vacuum.2023.111846

[14] I. Campos, M. Islas, E. González, P. Ponce, G. Ramírez, Use of fuzzy logic for modeling the growth of Fe2B boride layers during boronizing, Surf. Coat. Technol., 201 (6) (2006) 2717-2723. https://doi.org/10.1016/j.surfcoat.2006.05.016

[15] M. Ortiz-Domínguez, I. Campos-Silva, E. Hernández-Sánchez, J. L. Nava-Sánchez, J. Martínez-Trinidad, M. Y. Jiménez-Reyes, O. Damián-Mejía, Estimation of Fe_2B growth on low-carbon steel based on two diffusion models, Int. J. Mater. Res., 102 (4) (2011) 429-434. https://doi.org/10.3139/146.110491

[16] M. Ortiz-Domínguez, M. Keddam, Modelling boron diffusion for Fe_2B layer formation: comparative kinetics analysis in pack-boronized AISI 4147 steel, Mater. Test., 65 (10) (2023) 1539-1550. https://doi.org/10.1515/mt-2023-0214

[17] H. Kunst, O. Schaaber, Beobachtungen beim Oberflaechen-borieren von Stahl. Haerterei-Tech. Mitt., 22 (1) (1967) 1-25. (In German)

[18] ASTM International, ASTM C1327–15: Standard Test Method for Vickers Indentation Hardness of Advanced Ceramics. West Conshohocken, PA, USA: ASTM International, 2015.

[19] V. N. Vigdorovich, A.Y. Nashel'skii, Microhardness testing procedure and effect of composition on the microhardness of brittle materials, Soviet Powder Metal. Met. Ceram., 2 (1963) 123-127. https://doi.org/10.1007/BF01111826

[20] W. C. Oliver, G. M. Pharr, An improved technique for determining hardness and elastic modulus using load and displacement sensing indentation experiments, J. Mater. Res., 7 (1992) 1564-1583. https://doi.org/10.1557/JMR.1992.1564

[21] M. Ortiz-Domínguez, M. Keddam, M. Elias-Espinosa, M. Ramírez-Cardona, A. Arenas-Flores, J. Zuno-Silva, F. Cervantes-Sodi, E. Cardoso-Legorreta, Characterization and boriding kinetics of AISI T1 steel, Metall. Res. Techno., 116 (1) (2019) 102. https://doi.org/10.1051/metal/2018081

[22] H. Okamoto, B-Fe (boron-iron), J. Phase Equilib. Diff., 25 (2004) 297-298. https://doi.org/10.1007/s11669-004-0128-3

[23] M. Carbucicchio, L. Bardani, G. Palombarini, Mössbauer and metallographic analysis of borided surface layers on Armco iron, J. Mater. Sci., 15 (1980) 711-719. https://doi.org/10.1007/BF00551738

[24] S. R. G. Krishnan, P. Muthia , M. Jaganathan, Optimization of boriding process on AISI 1015 steel using response surface methodology, Matéria (Rio J.), 28 (2) (2023) 1-12. https://doi.org/10.1590/1517-7076-RMAT-2023-0086

[25] S. Demirci, M. M. Tünçay, Growth kinetics of borided 316L stainless steel obtained by selective laser melting, J. Cent. South Univ., 32 (2025) 332-349. https://doi.org/10.1007/s11771-024-5733-1

[26] L. Sánchez-Fuentes, S. Matias-Gutierres, E. I. García-Otamendi, H. D. Sánchez-Chávez, E. D. García-Bustos, M. A. Doñu-Ruiz, N. López-Perrusquia, Morphological Characterization of Fe_2B Borided Layers on AISI 9254 Steel Using Reused Boron Paste: A

Classical and Fractal Approach, Coatings, 15 (11) (2025) 1301. https://doi.org/10.3390/coatings15111301

[27] M. Kul, Y. Yılmaz, K. Oğuz Oskay, L. Cenk Kumruoğlu, Effect of chemical composition of boriding agent on the optimization of surface hardness and layer thickness on aisi 8620 steel by solid and liquid boriding processes, Adv. Mater. Sci., 22 (3) (2022) 14-22. https://reference-global.com/download/article/10.2478/adms-2022-0010.pdf

[28] M. Kulka, Trends in thermochemical techniques of boriding, in Current Trends in Boriding, Engineering Materials, Cham, Switzerland, Springer, 2019, p. 17-98.

[29] I. Türkmen, E. Yalamaç, Effect of alternative boronizing mixtures on boride layer and tribological behaviour of boronized SAE 1020 steel, Met. Mater. Int., 28 (2022) 1114-1128. https://doi.org/10.1007/s12540-021-009878

[30] K. Genel, I. Ozbek, C. Bindal, Kinetics of boriding of AISI W1 steel, Mater. Sci. Eng. A, 347 (1-2) (2003) 311-314. https://doi.org/10.1016/S0921-5093(02)00607-X

[31] Y. Li, K. Mao, H. Li, Evolution of Microstructure and Surface Property of 18CrNiMo7-6 Steel During Vacuum High-Temperature Boriding Process, Coatings, 16 (2) (2026) 149. https://doi.org/10.3390/coatings16020149

[32] O. Delai, C. Xia, L. Shiqiang, Growth kinetics of the FeB/Fe_2B boride layer on the surface of 4Cr5MoSiV1 steel: experiments and modelling, J. Mater. Res. Technol., 11 (2021) 1272-1280. https://doi.org/10.1016/j.jmrt.2021.01.109

[33] G. Çelebi Efe, M. İpek, İ. Özbek, C. Bindal, Kinetics of borided 31CrMoV9 and 34CrAlNi7 steels, Mater. Charact., 59 (1) (2008) 23-31. https://doi.org/10.1016/j.matchar.2006.10.007

[34] M. A. Borik, V. R. Borichevskij, V. T. Bublik, T. V. Volkova, A. V. Kulebyakin , E. E. Lomonova, F. Milovich, V. A. Myzina, P. A. Ryabochkina, S. V. Seryakov, N. Yu. Tabachkova , Anisotropy of mechanical properties and hardening mechanism in ZrO2–Y2O3 solid solution crystals, Mod. Electron. Mater., 3 (4) (2017) 142–147. https://doi.org/10.1016/j.moem.2017.11.004

[35] J. Chevalier, L. Gremillard, A. V. Virkar, D. R. Clarke, The tetragonal-monoclinic transformation in zirconia: lessons learned and future trends, J. Am. Ceram. Soc., 92 (9) (2009) 1901-1920. https://doi.org/10.1111/j.1551-2916.2009.03278.x

[36] N. Makuch, M. Kulka, M. Keddam, A. Piasecki, Growth kinetics, microstructure evolution, and some mechanical properties of boride layers produced on X165CrV12 tool steel, Materials, 16 (1) (2022) 26. https://doi.org/10.3390/ma16010026

[37] M. Kulka, N. Makuch, A. Piasecki, Nanomechanical characterization and fracture toughness of FeB and Fe_2B iron borides produced by gas boriding of Armco iron, Surf. Coat. Technol., 325 (2017) 515-532. https://doi.org/10.1016/j.surfcoat.2017.07.020

[38] G. Rodríguez-Castro, I. Campos-Silva, E. Chávez-Gutiérrez, J. Martínez-Trinidad, E. Hernández-Sánchez, A. Torres-Hernández, Mechanical properties of FeB and Fe_2B layers estimated by Berkovich nanoindentation on tool borided steel, Surf. Coat. Technol., 215 (2013) 291-299. https://doi.org/10.1016/j.surfcoat.2012.05.145

[39] O. A. Gómez-Vargas, M. Keddam and M. Ortiz-Domínguez. Kinetics and tribological characterization of pack-borided AISI 1025 Steel, High Temp. Mater. Proc., 36 (3) (2017) 197-208. https://doi.org/10.1515/htmp-2015-0199

[40] İ. Türkmen, E. Yalamaç, M. Keddam. Investigation of tribological behaviour and diffusion model of Fe2B layer formed by pack-boriding on SAE 1020 steel, Surf. Coat. Technol., 377 (2019) 124888. https://doi.org/10.1016/j.surfcoat.2019.08.017

[41] E. Hernández-Sánchez, J. C. Velázquez, J. L. Castrejón-Flores, A. Chino-Ulloa, I. P. Torres Avila, R. Carrera-Espinoza, J. A. Yescas-Hernández, C. Orozco-Alvarez, Tribological Behavior of Borided AISI 316L Steel with Reduced Friction Coefficient and Enhanced Wear Resistance, Mater. Trans., 60 (1) (2019) 156-164. https://doi.org/10.2320/matertrans.M2018282

[42] A. López-Leyva, J.L. Rosales-Lopez, P. Šulhánek, M. Olivares-Luna, I. Mejía-Caballero, P. Gogola, P. Jurči, I. Campos-Silva, The impact of post-treatments on the brittleness and wear resistance of borided 8 % Cr steel, Mater. Chem. Phys., 313 (2024)

128719. https://doi.org/10.1016/j.matchemphys.2023.128719.

[43] S. Tlili, S. Bouyegh, A. Daoui, A. Guedri, M. Tlili, L. Tairi, M. Djama, R. Graine ,

D. Charmati, Investigation on microstructure and mechanical properties of boron-modified 13Cr5Ni2Mo by powder-pack boriding, Mater. Sci. Technol., 39 (18) (2023) 3209-3219. https://doi.org/10.1080/02670836.2023.2245657

[44] S. İ. Ayvaz, Investigation of the effect of boriding on the wear behaviour of AISI 1050 carbon steel, Int. Adv. Res. Eng. J., 7 (1) (2023) 1-7. doi: 10.35860/iarej.1122159.

[45] İ. Türkmen, C. Gül, F. Sargın, K. Kanbur, Effect of boronizing parameters on mechanical and tribological characteristics of Monel K-500 super alloy, J. Alloys Compd., 1036 (2025) 182077. https://doi.org/10.1016/j.jallcom.2025.182077.

[46] G. Kara and G. Pürçek, Effects of boride coating on wear behaviour of biomedical grade Ti–45Nb alloy, Mater. Test., 67 (7) (2025) 1158-1167. https://doi.org/10.1515/mt-2025-0030

[47] H. Attar, S. Ehtemam-Haghighi, D. Kent, I. V. Okulov, H. Wendrock, M. Bönisch, A. S. Volegov, M. Calin, J. Eckert, M. S. Dargusch, Nanoindentation and wear properties of Ti and Ti-TiB composite materials produced by selective laser melting, Mater. Sci. Eng. A, 688 (2017) 20-26. https://doi.org/10.1016/j.msea.2017.01.096

[48] Y. Kayali, R. Kara, Investigation of Wear Behavior and Diffusion Kinetic Values of Boronized Hardox-450 Steel, Prot. Met. Phys. Chem. Surf., 57 (2021) 1025-1033. https://doi.org/10.1134/S2070205121050129

[49] I. Gunes, S. Ulker, S. Taktak, Kinetics of plasma paste boronized AISI 8620 steel in borax paste mixtures, Prot. Met. Phys. Chem. Surf., 49 (2013) 567-573. https://doi.org/10.1134/S2070205113050122

[50] G. Kartal Sireli, H. Yuce, M. Arslan, M. Karimzadehkhoei, S. Timur, Improving the Surface Performance of Discarded AISI T1 Steel by Cathodic Reduction and Thermal Diffusion-Based Boriding, J. Mater. Eng. Perform., 32 (2023) 9504-9514. https://doi.org/10.1007/s11665-023-07817-5

[51] Y. Kayali, Investigation of the Diffusion Kinetics of Borided Stainless Steels, The Phys. Met. Metallogr., 114 (2013) 1061-1068.https://doi.org/10.1134/S0031918X1322002X

[52] S. İ. Ayvaz, D. Zalaoğlu, E. Özer, A. İ. Bahçepınar, İ. Aydın, Determination of diffusion kinetics, wear and corrosion behaviour of boro-sintered powder metal AISI 316 stainless steel alloy, Surf. Interfaces, 62 (2025) 106164. https://doi.org/10.1016/j.surfin.2025.106164

[53] A. Mourad, A., A.A. Mahdy, E.S. Mosa, A. Kandil, M. A. Elhelaly, Enhancement of tribological behavior and microhardness of AISI H13 tool steel by electrochemical boriding, Sci. Rep., 15, (2025) 43384. https://doi.org/10.1038/s41598-025-28422-7

[54] M. Ortiz-Domínguez, M. Keddam, Á. J. Morales-Robles, Characterizations and boron diffusion modelling on the AISI H13 steel, J. Min. Metall. Sect. B-Metall., 60 (3) (2024) 353-365. https://doi.org/10.2298/JMMB240423029O

[55] J. Zuno-Silva, M. Ortiz-Domínguez, M. Keddam, M. Elias-Espinosa, O. Damián-Mejía, E. Cardoso-Legorreta, M. Abreu-Quijano, Boriding kinetics of Fe_2B layers formed on AISI 1045 steel, J. Min. Metall. Sect. B-Metall., 50 (2) (2014) 101-107. https://doi.org/10.2298/JMMB140323019Z

Figure captions

Figure 1. *Experimental setup used for the pack-boriding treatment. It includes: (1) a lid with a small opening for the release of gaseous species, (2) the powder mixture used, (3)*

the sample to be treated, and (4) the main cylindrical body of the container. All dimensions are given in mm.

Figure 2. Schematic representation of the experimental methodology employed for the preparation, thermochemical treatment, metallographic processing, and microstructural characterization of ASTM A29 steel.

Figure 3. *Classification system used to assess the brittleness of borided surfaces, including indicators of additional damage around the indentation.*

Figure 4. *The* ***generated*** *Fe_2B layer along with the B distribution accross it.*

Figure 5. *SEM micrographs showing the Fe_2B layers on the ASTM A29 steel obtained at different temperatures for 6 h: (a) 1123 K, (b) 1173 K, (c) 1223 K, and (d) 1273 K.*

Figure 6. *SEM images of cross-sections of boride layers obtained at 1273 K for 8 h along with the EDS analyses in two distinct locations: (a) near the top surface, (b) at the (boride layer/substrate) interface.*

Figure 7. *XRD diffractograms of borided surfaces of ASTM A 29 steel at 1273 K for different treatment times : (a) 4 h, (b) 6 h, and (c) 8 h.*

Figure 8. *Optical images showing the Vickers indents along the boride layers for two different loads and processing parameters : (a) 6 h at 1223 K under a load of 50 gf, and (b) 4 h at 1273 K under a load of 100 gf.*

Figure 9. *Behaviour of Fe_2B layers formed on ASTM A29 steel (1273 K for 4 h) under two applied loads using a Vickers indenter: (a) 50 gf and (b) 100 gf.*

Figure 10. *SEM images of indents and nanoindentation curves for two processing parameters (a) steel borided at 1223 K for 6 h and (b) steel borided at 1273 K for 4 h.*

Figure 11*. Evolution of the friction coefficient as a function of sliding distance for two ASTM A29 steel surfaces: borided (1273 K for 8 h) and unborided.*

Figure 12. *Wear scar profiles of untreated and surface-hardened ASTM A29 steel after boriding at 1273 K for 8 h..*

Figure 13. *Kinetic analysis of Fe_2B layer growth over time.*

Figure 14. *SEM micrographs of cross-section of borided ASTM A29 steels for 4 additional processing parameters: (a) 1173 K for 9 h, (b) 1223 K for 3 h, (c) 1223 K for 4.5 h and (d) 1273 K for 5 h.*

Table captions

Table 1. *Chemical composition of ASTM A29 steel expressed in weight percent (wt.%)*

Table 2. *Experimental* k values with the incubation times in the temperature range *1123-1273 K.*

Table 3. *Assessed B diffusion coefficients in* Fe_2B *with the Taylor expansion model.*

Table 4. *Comparative analysis of the differences in activation energy values.*

Table 5. *Experimental verification of the Taylor expansion model using four boriding conditions.*